

# 1 Wireless Communication with Nanoplasmonic Data Carriers: 2 Macroscale Propagation of Nanophotonic Plasmon Polaritons 3 Probed by Near-Field Nanoimaging

4 Moshik Cohen,<sup>\*,†,§</sup> Yossi Abulafia,<sup>§</sup> Dmitry Lev,<sup>||</sup> Aaron Lewis,<sup>||</sup> Reuven Shavit,<sup>‡</sup> and Zeev Zalevsky<sup>†,§</sup>

5 <sup>†</sup>Faculty of Engineering, Bar-Ilan University, Ramat-Gan 52900, Israel

6 <sup>‡</sup>Department of Electrical and Computer Engineering, Ben-Gurion University of the Negev, Beer-Sheva 84105, Israel

7 <sup>§</sup>Bar-Ilan Institute for Nanotechnology & Advanced Materials, Ramat-Gan 52900, Israel

8 <sup>||</sup>Department of Applied Physics, Selim and Rachel Benin School of Engineering and Computer Science, The Hebrew University,  
9 Givat Ram, Jerusalem 9190401, Israel

10 **ABSTRACT:** The ability to control the energy flow of light at the nanoscale is  
11 fundamental to modern communication and big-data technologies, as well as quantum  
12 information processing schemes. However, because photons are diffraction-limited, efforts  
13 of confining them to dimensions of integrated electronics have so far proven elusive. A  
14 promising way to facilitate nanoscale manipulation of light is through plasmon  
15 polaritons—coupled excitations of photons and charge carriers. These tightly confined  
16 hybrid waves can facilitate compression of optical functionalities to the nanoscale but suffer  
17 from huge propagation losses that limit their use to mostly subwavelength scale  
18 applications. With only weak evidence of macroscale plasmon polaritons, propagation has  
19 recently been reported theoretically and indirectly, no experiments so far have directly  
20 resolved long-range propagating optical plasmon polaritons in real space. Here, we launch  
21 and detect nanoscale optical signals, for record distances in a wireless link based on novel  
22 plasmonic nanotransceivers. We use a combination of scanning probe microscopies to  
23 provide high resolution real space images of the optical near fields and investigate the long-  
24 range propagation of nanoscale optical signals. We design our nanotransceivers based on a high-performance nanoantenna,  
25 *Plantenna*, hybridized with channel plasmon waveguides with a cross-section of 20 nm × 20 nm, and observe propagation for  
26 distances up to 1000 times greater than the plasmon wavelength. We experimentally show that our approach hugely outperforms  
27 both waveguide and wireless nanophotonic links. This successful alliance between *Plantenna* and channel plasmon waveguides  
28 paves the way for new generations of optical interconnects and expedites long-range interaction between quantum emitters and  
29 photomolecular devices.



30 **KEYWORDS:** Plasmonics, nanoantennas, channel waveguides, wireless, nanoimaging

31 **T**he proposed scheme is designed to enable macroscale  
32 communication between nanoscale devices utilizing  
33 surface plasmon polaritons (SPPs). Hence, we use channel  
34 waveguides that confine SPPs to their channel dimensions,  
35 which can be as small as several nanometers.<sup>1–8</sup> However, as  
36 dimensions decrease, SPPs exhibit increased losses that limit  
37 their propagation in waveguides to distances of only few  
38 micrometers. To address this fundamental limitation, we  
39 convert channel SPPs to optical surface waves that propagate  
40 for significantly larger distances on dielectric substrates. A high-  
41 efficiency nanoreceiver, designed to convert surface waves to  
42 channel SPPs, is placed the remote edge of the system. **Figure**  
43 **1a** illustrates the proposed communication nanosystem, which  
44 (a) converts light to nanoscale SPPs, (b) propagates SPPs in  
45 channel waveguide, (c) converts these SPPs to surface waves  
46 and propagate them for long distance, and (d) excites SPPs  
47 from the surface waves at remote locations. As shown in the  
48 right-hand side of **Figure 1a**, laser light illuminates the  
49 *Plantenna* to launch SPPs at the waveguide. Second, *Plantenna*,

located at the other edge of the waveguide, converts these SPPs 50  
to surface waves that propagate on the substrate. The surface 51  
waves are reconverted to SPPs at a remote, *Plantenna* based 52  
nanoreceiver. We use waveguides with a propagation loss of 53  
 $e^{-\alpha l}$ , where the absorption constant  $\alpha = (18 \mu\text{m})^{-1}$  for a 54  
channel width of 20 nm at a red wavelength of  $\lambda = 633 \text{ nm}$  and 55  
 $l$  is the propagation length. 56

In contrast, absorption for wireless links occur only at the 57  
antennas and are much lower than for a waveguide. For 58  
conventional (e.g., dipole, bowtie) nanoantennas, the prop- 59  
agation loss for wireless links behaves like  $(D/l)^2$ , where  $D$  is 60  
the directivity.<sup>9</sup> Here, we show that *Plantenna* based wireless 61  
links hugely outperform both waveguide and conventional 62  
nanoantenna based alternatives. **Figure 1b** presents a 3D model 63  
of the nanotransceiver, with zoom in to the *Plantenna* region 64

**Received:** January 19, 2017

**Revised:** April 25, 2017

**Published:** May 3, 2017

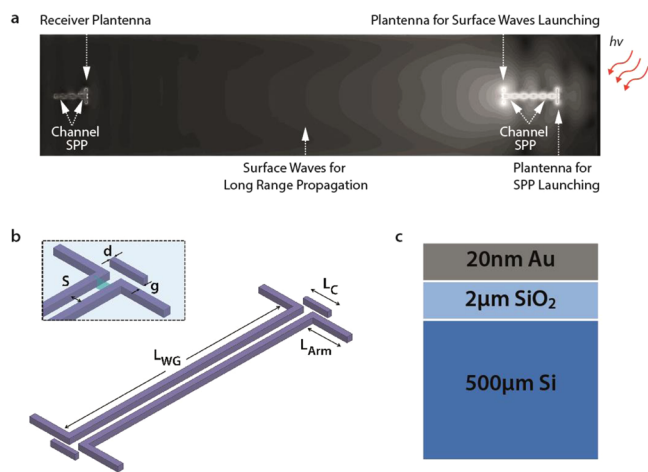


**Figure 1.** Wireless communications with optical plasmon polaritons. (a) Illustration of the proposed nanoscale communication system. SPP launching Plantenna (right) converts free space light to propagating waveguides SPPs, which are coupled to surface waves by the “Surface Waves Launching Plantenna” for long-range propagation. A Plantenna based nanoreceiver (left) converts the surface waves to channel SPPs at remote distances. (b) 3D model of a Plantenna based plasmonic nanotransceiver. Zoom in to the Plantenna region is shown in the inset c, materials stack up used to fabricate the devices.

65 shown in the inset. The physical principle behind the Plantenna  
 66 invention is the enormous field enhancement and confinement  
 67 exhibited by resonant, optically illuminated adjacent metallic  
 68 nanoparticles. These properties, mainly originated from  
 69 coherent capacitive coupling between the particles, are  
 70 significantly better than those of isolated nanoparticles. The  
 71 Plantenna comprised of two metallic nanorods of length  $L_{Arm}$ ,  
 72 separated by a nanoscopic gap ( $s = 10\text{--}35\text{ nm}$ ), in a dipole  
 73 arrangement. An additional nanorod, termed director, is placed  
 74 at much closer proximity of only 7 nm ( $g \sim 7\text{ nm}$ ) to the  
 75 dipole. A detailed analysis on the Plantenna physics, which also  
 76 includes optimization for high efficiency excitation of channel  
 77 SPPs, was recently reported.<sup>5</sup> Figure 1c shows the material  
 78 stack up used in this work, comprised of 20 nm Au layer  
 79 deposited on a Si on insulator (SOI) wafer ( $500\text{ }\mu\text{m Si}$ ,  $2\text{ }\mu\text{m}$   
 80  $\text{SiO}_2$ ), for potential CMOS computability.

81 For nanofabrication, we use electron beam lithography  
 82 (EBL), ion beam sputtering (Au, 20 nm), and liftoff. After  
 83 liftoff, the resist is completely removed, allowing contact mode  
 84 near-field optical characterization. We fabricated devices  
 85 comprised of standalone nanotransceivers and complete  
 86 communication systems. Figure 2a shows a high-resolution  
 87 scanning electron microscopy (HR-SEM) image of a fabricated  
 88 nanotransceiver, recorded at beam current of 0.4 nA and low  
 89 accelerating voltage of 5 kV, for sub 1 nm imaging resolution;  
 90 corresponding 3D AFM topography is shown in Figure 2b.  
 91 Nanotransceivers with dimensions of  $L_{Arm} = 220\text{ nm}$ ,  $L_C = 120$   
 92  $\text{nm}$ ,  $s = 20\text{ nm}$ ,  $g = 7\text{ nm}$ , and  $L_{WG} = 1.5\text{ }\mu\text{m}$  were fabricated  
 93 successfully and repeatedly. Figure 2c shows near-field KPFM  
 94 nanoimaging under illumination with a He–Ne laser ( $\lambda_0 = 633$   
 95  $\text{nm}$ ), recorded at a set lift height of 30 nm using a high aspect  
 96 ratio uncoated Si AFM tip with a diameter of 2 nm. As  
 97 observed, the laser light is efficiently converted to propagating  
 98 plasmons at the waveguide channel by the Rx (right) Plantenna  
 99 and then recoupled to surface waves via the Tx (left) Plantenna.  
 100 Characterized by periodic peaks (purple) in the KPFM signal  
 101 imaged at the waveguide channel, SPPs with an effective

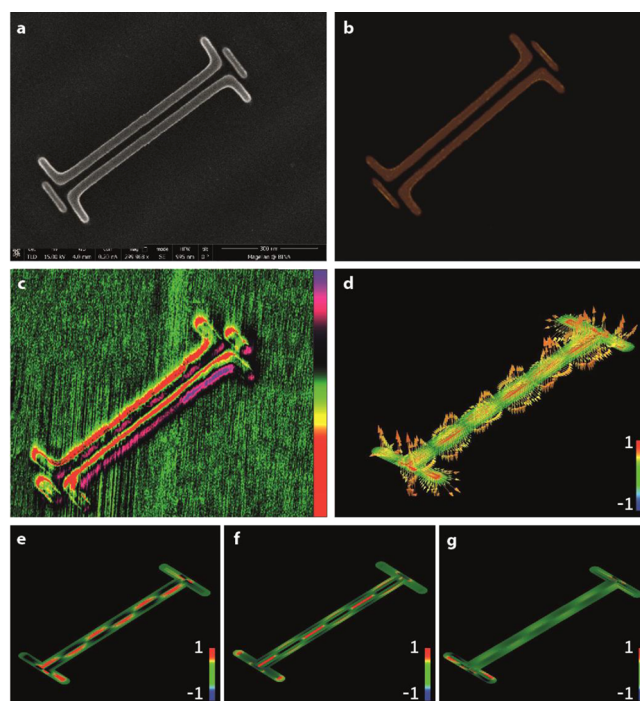


**Figure 2.** Plantenna-based plasmonic nanotransceiver. (a) High-resolution SEM image of the fabricated nanotransceiver. (b) 3D AFM image of the fabricated nanotransceiver. (c) KPFM under optical illumination analysis of the nanotransceiver. KPFM signal scale bar:  $\pm 4.7\text{ V}$ . (d) Numerically calculated optical near-field vector. (e) Numerically calculated optical near-field image showing  $\text{Re}(E_z) = |E_z| \cos(\phi_z)$ . (f) Numerically calculated optical near-field showing  $\text{Re}(E_x)$ . (g) Numerically calculated optical near field showing  $\text{Re}(E_y)$ . Scale bar: 100 nm.

wavelength of 35–150 nm were measured. The experimental  
 102 results are reproduced by numerical calculation results,  
 103 presented at the optical frequency of 474 THz (633 nm).  
 104 The theoretical results are obtained using a high-frequency  
 105 structure simulator based on the finite element method  
 106 (FEM).<sup>3–5,10,11</sup> Numerical calculation results of the device  
 107 are shown in Figure 2d–g, with Figure 2d showing the local  
 108 near-field vector in 3D, and Figure 2e–g presenting the scalar  
 109 component of the electrical near-field magnitudes  $\text{Re}\{|E_z|$ ,  
 110  $\text{Re}\{|E_x|$ , and  $\text{Re}\{|E_y|$ , respectively.  
 111

The analysis of a nanoscale wireless communication system  
 112 that transmits and receives optical plasmon polaritons with a  
 113 cross section of  $20\text{ nm} \times 20\text{ nm}$  to distance of  $12\text{ }\mu\text{m}$  is shown  
 114 in Figure 3. The system is comprised of a plasmonic  
 115 nanotransceiver (Figure 1b) and a nanoplasmonic receiver,  
 116 separated by a distance of  $12\text{ }\mu\text{m}$ . Figure 3a presents 3D AFM  
 117 topography mapping of the nanosystem, where the transceiver  
 118 is fabricated at the right-hand side and the receiver is located at  
 119 the left side. To image the near-field structure of long-range  
 120 plasmon polaritons transfer in real space, we use a combination  
 121 of KPFM and SNOM. KPFM enables near-field mapping of  
 122 plasmonic devices with a very high resolution. However, it has  
 123 limited efficiency in characterizing dielectric devices, mainly  
 124 since the work function of dielectric materials barely can be  
 125 modified by optical illumination.<sup>3,4,6,12</sup> Figure 3b shows KPFM  
 126 analysis of the nanosystem, illuminated by a He–Ne laser ( $\lambda =$   
 127  $633\text{ m}$ ), linearly polarized in parallel to the dipole orientation  
 128 and focused to diameter of 700 nm. Channel SPPs are observed  
 129 at the nanotransceiver channel waveguide, propagate for 130

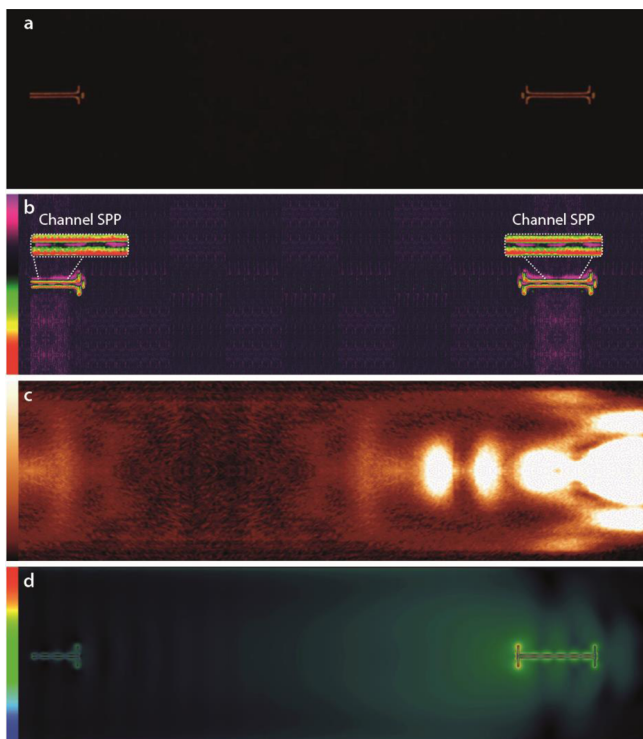


**Figure 3.** Characterization of the proposed wireless link, demonstrating efficient long-range propagation of tightly confined optical plasmon polaritons. (a) 3D AFM image of the fabricated wireless link system. (b) KPFM under optical illumination analysis of the wireless link system, showing SPPs at the transmission (right) and reception (left) sides; inset—zoom in to the respective waveguide channel. KPFM signal scale bar:  $\pm 4.7$  V. (c) SNOM analysis of the wireless link system, showing SPPs at the transmission (right) and reception (left) sides, as well as the coupling to surface waves that enable the long-range propagation. (d) Numerically calculated near-field image, showing the complete optical wireless transfer link. Scale bar: 750 nm.

distance of  $L_{WG} = 1 \mu\text{m}$ , followed by strong “hot spot” at the Tx 131  
Plantenna that converts them to surface waves. A zoom in to 132  
the channel region is presented in the inset, clearly showing the 133  
periodic structure of the excited SPPs. Remarkably, pronounced 134  
SPP excitation is observed at the distanced receiver, which is 135  
not illuminated by the laser. Highlighted in the left inset, the 136  
channel SPPs at the receiver waveguide are excited by efficient 137  
coupling of surface waves to SPP by the receiver Plantenna. 138  
The surface waves on the  $\text{SiO}_2$  surface are imaged in the near 139  
field via SNOM, as shown in Figure 3c. Naturally, SNOM 140  
provides lower resolution images compared to KPFM,<sup>3</sup> 141  
however, its direct optical imaging mechanism enables mapping 142  
of the surface photons that propagate on the dielectric medium, 143  
unlike KPFM. Note that the SNOM image exhibits high 144  
intensity at the physical locations of the transmitter and 145  
receiver, originated by plasmon excitation. Hence, we state that 146  
the combination of KPFM and SNOM provides a comple- 147  
mentary, complete real-space nanoimaging approach for the 148  
characterization of nanoscale wireless communication systems, 149  
which facilitates high-resolution nanoimaging of both plasmons 150  
and optical surface waves. Numerical calculation results of the 151  
nanosystem, presenting the electric near-field magnitude  $|\mathbf{E}|$ , are 152  
shown in Figure 3d. Both channel SPPs as well as the surface 153  
waves in the dielectric substrate are clearly captured, providing 154  
additional confirmation to our approach. 155

To unambiguously demonstrate the excellent efficiency of 156  
our Plantenna based nanosystem, we compare its performances 157  
to direct channel waveguiding link<sup>6–8,13</sup> and to wireless link 158  
based on dipole nanoantennas.<sup>14–17</sup> For the wireless link 159  
configurations (Figure 4a–d) the distance between the 160 f4  
transceiver and receiver is  $10 \mu\text{m}$ , and for the direct link 161  
(e.g., Figure 4e–f) the waveguide length is  $3 \mu\text{m}$ , limited by 162  
fabrication constraints. Figure 4a shows AFM image of our 163  
proposed Plantenna based nanosystem, as the corresponding 164  
KPFM mapping is shown in Figure 4b with a voltage scale bar 165  
of  $\pm 4.7$  V. Pronounced plasmon excitation is probed at the 166  
receiver, evidenced by the modal structure of the field inside 167

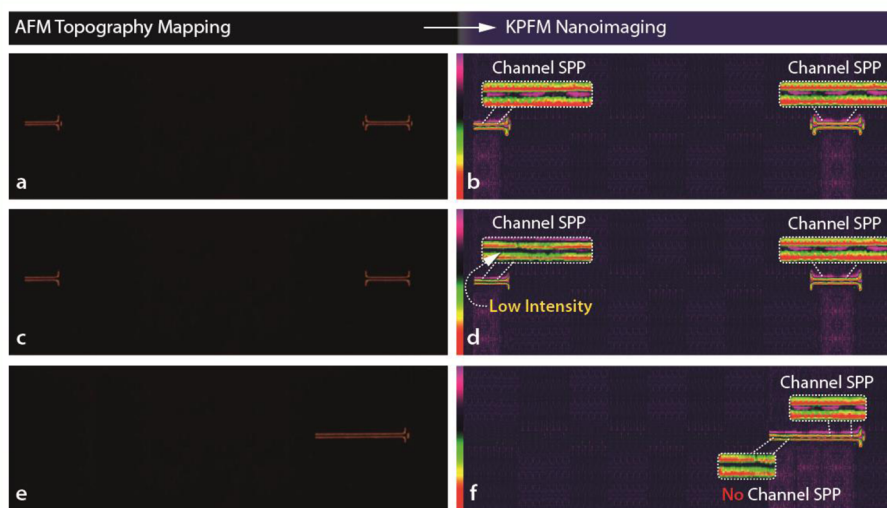


**Figure 4.** Comparison between nanophotonic links. (a) 3D AFM image of the Plantenna-based wireless link system. (b) KPFM under optical illumination analysis of the Plantenna-based wireless link system; KPFM signal scale bar:  $\pm 4.7$  V. (c) 3D AFM image of the dipole nanoantenna-based wireless link system. (d) KPFM under optical illumination analysis of the dipole nanoantenna-based wireless link system; KPFM signal scale bar:  $\pm 0.5$  V. (e) 3D AFM image of channel SPP waveguide with an identical cross section to the waveguides in a–d and  $3 \mu\text{m}$  length. (f) KPFM under optical illumination analysis of the channel SPP waveguide link; KPFM signal scale bar:  $\pm 4.7$  V; inset (b, d, f): zoom in to the respective waveguide channel. Scale bar:  $1 \mu\text{m}$ .

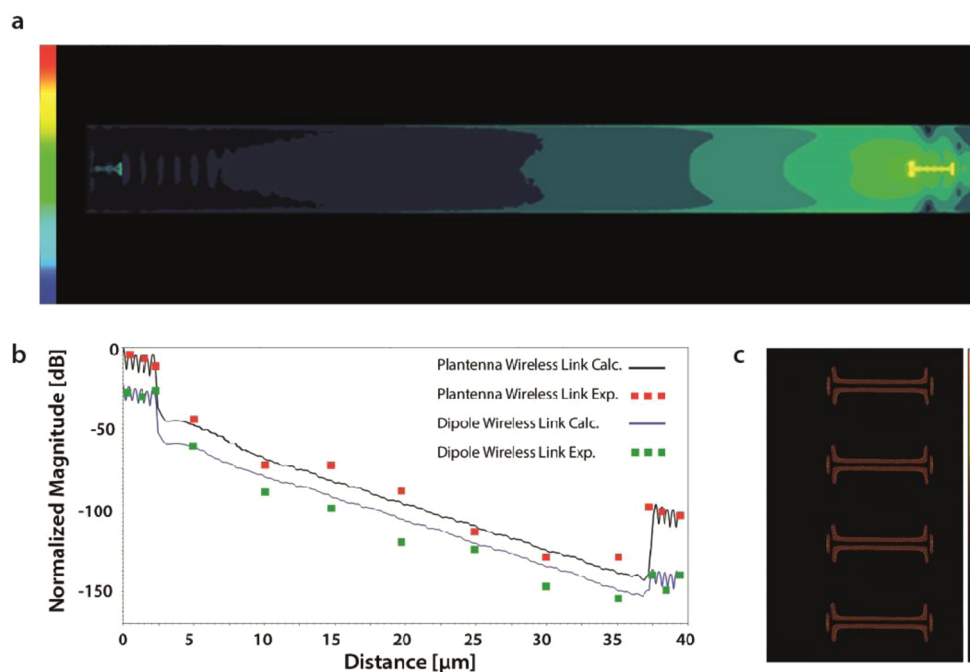


**Figure 5.** Performance analysis for ultralong propagation distances. (a) Numerically calculated near field image, showing the complete Plantenna-based wireless transfer link with distance of 35  $\mu\text{m}$  between the transmitting and receiving sides. (b) Performance comparison between Plantenna and dipole based wireless links for 35  $\mu\text{m}$ , showing a 30 dB better performance of the Plantenna configuration. (c) 3D AFM image of a three-element Plantenna based transceiver phased array. Scale bar: 200 nm.

168 the channel which is highlighted in the inset. Figure 4c shows  
 169 the AFM topography of a wireless link based on dipole  
 170 nanoantennas, which was recently proposed as an approach for  
 171 plasmonic energy transfer;<sup>18</sup> the corresponding KPFM image is  
 172 presented in Figure 4d with a voltage scale bar of  $\pm 0.5$  V.

173 We observe plasmon excitation at the transceiver; however,  
 174 significantly less noticeable intensity is measured at the receiver  
 175 waveguide (see inset) compared with the Plantenna based  
 176 architecture. Figure 4e shows a 3D AFM image of a Plantenna  
 177 integrated with a similar waveguide of 3  $\mu\text{m}$  length,  
 178 implementing a direct nanoplasmonic link. Unlike the wireless  
 179 links, the waveguide exhibits much higher propagation loss  
 180 since it directly propagates tightly confined plasmons that  
 181 interacts with the metals in their entire guided route.<sup>18</sup> A  
 182 KPFM map of the direct link is shown in Figure 4f (scale bar  
 183  $\pm 4.7$  V), where the zoom in to the different channel regions is  
 184 presented in the insets. As seen in the right inset, channel SPPs  
 185 are excited by the Plantenna and propagate through the  
 186 waveguide. However, the huge propagation loss makes the  
 187 waveguide SPPs decay significantly and being practically  
 188 unobservable after propagating for only 2.5  $\mu\text{m}$ , as seen in  
 189 the left inset of Figure 4f. This reconfirms the critical, huge  
 190 losses exhibited in gap plasmon waveguides with nanoscale  
 191 channels, which hamper their real life applicability. Figure 5a  
 192 shows the calculated electric near field for a Plantenna based  
 193 communication nanosystem with a 35  $\mu\text{m}$  distance between the  
 194 transmitter and receiver. Even for this high separation, plasmon  
 195 excitation is clearly observed in the receiving device. Dipole  
 196 nanoantenna is the most popular form of compact couplers to  
 197 channel waveguide, enabling us to achieve 200 times higher  
 198 efficiency compared with the case of directly illuminating a base  
 199 waveguide.<sup>3,4,6,7,10,16</sup> Other types of couplers may use nano-  
 200 focusing approaches<sup>15</sup> or more complex coupling devices like a  
 201 Yagi nanoantenna.<sup>19</sup> However, these devices are diffraction  
 202 limited and cause only marginal improvement compared with

the dipole coupler. A comparison between Plantenna and 203  
 dipole based systems with 35  $\mu\text{m}$  separation is shown in Figure 204  
 5b, presenting the normalized near field along a line that 205  
 connects the transmitter and receiver passing through the 206  
 centers of both waveguides. The continuous black and blue 207  
 charts represent the calculated results of a Plantenna and dipole 208  
 wireless systems, respectively, as the discrete red and green 209  
 squared dots are the corresponding experimental results. High 210  
 field values are observed in both Tx and Rx ends, attributed to 211  
 plasmon enhancement by the nanoantennas. As expected, the 212  
 field is attenuated linearly when propagates through the SiO<sub>2</sub> 213  
 substrate. 214

A quantitative comparison between Plantenna and dipole 215  
 systems is performed by comparing the SPP magnitude at both 216  
 receiver waveguides, which serve as input for remote nano- 217  
 plasmonic circuits<sup>4,12,20</sup> or can be probed by photoelectric 218  
 detectors. Since both systems are excited with identical sources 219  
 and use similar plasmon waveguides, this approach is equivalent 220  
 to calculating the ratio between the wave power of the SPP at 221  
 the receiver waveguide and the laser source. As seen in Figure 222  
 5b, the Plantenna based nanosystem outperforms the dipole 223  
 configuration by more than 30 dB. Note that from nano- 224  
 fabrication considerations we use Plantenna with identical 225  
 dimensions through all of the experiments herein. However, the 226  
 additional significant efficiency improvement can be achieved 227  
 using a structural optimization of the different Plantennas as we 228  
 recently reported.<sup>5</sup> The Plantenna nanosystem can be used to 229  
 wirelessly transfer optical nanoplasmonic information for 230  
 macroscale distances using a phased array<sup>21–24</sup> configuration 231  
 as shown in Figure 5c. By fabricating an array of identical 232  
 transceivers spaced by  $\lambda_0/2$  ( $\lambda_0$  is the free space wavelength), 233  
 the emitted surface waves coupled from all of the transceivers 234  
 can be coherently combined on the surface. Based on the well- 235  
 known Friis principle,<sup>18,25,26</sup> the phased array architecture 236  
 enables propagation distances which are linearly scalable with 237

the number of transceivers, paving the way toward efficient wireless nanoplasmonic data and energy transfer for millimeter distances and beyond.

In conclusion, we designed, fabricated, and experimentally characterized a novel high-efficiency nanosystem, capable to wirelessly transfer deeply confined optical plasmon polaritons for chip-scale distances. Our system is architected for the efficient conversion of nanoscopic SPPs to propagating surface waves and to re-excite SPPs from these surface waves at significantly remote distances. We demonstrate the transmission of optical SPPs in channel waveguides with a cross section of only  $20\text{ nm} \times 20\text{ nm}$ , for distances which are 3 orders of magnitude larger than the plasmon wavelength. On the basis of the Plantenna, a new generation of high-performance nanoantennas with no RF equivalents, our nanosystem hugely outperforms both direct and wireless links based on dipole nanoantennas by more than 30 dB. For the first time, we use a unique combination of scanning probe microscopies to create complete real-space near-field mapping of a long-range nanoplasmonic wireless link at a high spatial resolution. This nanoimaging amalgamation provides valuable synergy needed for mapping both nanoscopic plasmon polaritons as well as macroscopically propagating surface waves. In the quest for reconciling the dimensional mismatch between diffraction-limited photonics and integrated electronics, our results enable new horizons for high integration densities of optical functionalities and interconnects. By using phased array configuration and utilizing degrees of freedom in polarization, frequency and code domains, inter- and intra-chip communications based on ultrafast nanoscale light waves as information carriers can now achieve record performances in terms of speed distance and size. The presented approach of hybridizing Plantenna and channel plasmon waveguides as nanotransceivers is immediately applicable for exploring long-range interaction between single and multiple quantum emitters, while our nanoimaging methodology enables enhanced understanding of exciting near-field phenomena at the nanoscale.

**Methods. AFM and KPFM Measurements.** All measurements were performed at room temperature and free ambient conditions (no vacuum), using a Dimension Icon AFM system with a NanoScope V controller (Bruker). For both AFM and KPFM measurements, we used NanoWorld probes SSS-NCH (SuperSharpSilicon, Noncontact/Tapping mode, High resonance frequency), with a typical diameter of 2 nm, resonance frequency of 320 kHz, and spring constant of 42 N/m. Typically, voltages of 2 V, AC capacitance frequencies of 880 MHz, lift heights of 30–50 nm, and line rates of 0.1 kHz were employed. To map the CPD of the sample, we apply both AC voltage (VAC) and DC voltage (VDC) to the AFM tip. VAC generates oscillating electrical forces between the AFM tip and sample surface, and VDC nullifies the oscillating electrical forces that originated from CPD between tip and sample surface.

**Optical Near-Field Measurements.** The optical characterization of the plasmonic structures was performed by a MultiView 2000 scanning probe microscope/NSOM system (Nanonics Imaging Ltd.). The SPM head was placed on the stage of an Olympus dual microscope while remaining the optical axis free from above and below. Such a configuration allowed us to bring the cantilevered NSOM tip to the desired position on the sample under an upper objective of 50X. The sample was illuminated with a Liconix diode laser of 785 laser

CW light from the bottom and focused on a sample with a  $50\times$  objective. We used the bottom piezo scanner of the scanning head to place the desired structures of the sample very accurately relatively to the incoming light of the laser from below. The scan was performed with upper piezo scanner allowing moving only the NSOM tip while the sample remains still. The collection of near field light distribution on the surface was performed in tapping mode with a 200 nm aperture NSOM tips based tuning fork produced by Super Tips (Nanonics Imaging Ltd.). The signal was transmitted through a multimode optical fiber onto an APD. The AFM and NSOM images were collected simultaneously during the scan, allowing to monitor the topography of the desired structure and to correlate it with the near-field optical signal that comes from any particular feature.

**Numerical Simulations.** The numerical results are obtained by using the software package ANSYS HFSS V15, the industry-standard simulation tool for 3D full-wave electromagnetic field simulation. HFSS solves Maxwell's equations via the finite element method (FEM) using an adaptive mesh refinement process for tailored accuracy requirements. The field's solutions are calculated with the metallic (Ag) plasmonic structures being deposited on a homogeneous  $\text{SiO}_2$  substrate. The nanoantenna is illuminated by optical sources at 474 THz (wavelength of 633 nm), which are modeled as focused Gaussian beams with 1  $\mu\text{m}$  characteristic diameter. The electric field is polarized in parallel with the dipole direction, as the wave vector  $\mathbf{K}$  is perpendicular. A selectively dense meshing is assigned in the metallic and waveguiding regions, with a maximum cell size of 1 nm and 750 000 FEM tetrahedral cells. To provide maximum accuracy, the model is terminated as following: the interface with free space is bounded by perfectly matched layer (PML) absorbing boundary conditions (ABC), while the metallic and  $\text{SiO}_2$  termination are done via layered impedance (LI) ABC. The minimum number of adaptive meshing iterations was set to 12, with a convergence condition of 1% maximum energy variance between adjacent iterations.

**Fabrication.**  $\text{SiO}_2/\text{Si}$  sample was spin-coated with poly(methyl methacrylate) (PMMA 950 A2) electron-beam resist providing thickness of 100 nm. The samples coated with PMMA were subsequently baked for 120 s on a hot plate at 180C. The desired pattern was exposed in the PMMA layer using a CRESTEC CABLE-9000C high-resolution electron-beam lithography system using different doses to control line and gap width. Then the samples were developed for 90 s using methyl isobutyl ketone (MIBK) and rinsed with IPA. The samples were subsequently exposed to Ar plasma to etch 10 nm in order to remove leftovers from the pattern, sputtered using BESTEC 2" DC magnetron to deposit 2 nm Cr and 18 nm Au, and then immersed in 180 KHz ultrasonic bath with NMP for 3 h for resist liftoff.

## AUTHOR INFORMATION

### Corresponding Author

\*E-mail: [moshik.cohen80@gmail.com](mailto:moshik.cohen80@gmail.com).

### ORCID

Moshik Cohen: [0000-0002-7519-9742](https://orcid.org/0000-0002-7519-9742)

### Author Contributions

M.C. carried out the theoretical design and analysis, designed the studies, performed the experiments, and wrote the manuscript. Z.Z. and R.S. participated in writing the manuscript and designing the study.

362 **Notes**

363 The authors declare no competing financial interest.

364 ■ **ACKNOWLEDGMENTS**

365 M.C. acknowledges Olga Girshevitz Yafit from Bar-Ilan  
366 Institute for Nanotechnology & Advanced Materials (BINA),  
367 for the support in fabricating the reported structures.

368 ■ **REFERENCES**

- 369 (1) Schuller, J. A.; Barnard, E. S.; Cai, W.; Jun, Y. C.; White, J. S.;  
370 Brongersma, M. L. *Nat. Mater.* **2010**, *9* (3), 193–204.
- 371 (2) Brongersma, M. L.; Shalae, V. M. *Science* **2010**, *328* (5977),  
372 440–441.
- 373 (3) Cohen, M.; Shavit, R.; Zalevsky, Z. *Sci. Rep.* **2015**, *4*, 04096.
- 374 (4) Cohen, M.; Zalevsky, Z.; Shavit, R. *Nanoscale* **2013**, *5* (12),  
375 5442–5449.
- 376 (5) Cohen, M.; Shavit, R.; Zalevsky, Z. *Sci. Rep.* **2015**, *5*, 17562.
- 377 (6) Cohen, M.; Shavit, R.; Zalevsky, Z. In *Planar Waveguides and*  
378 *other Confined Geometries*; Marowsky, G., Ed.; Springer Series in  
379 Optical Sciences; Springer: New York, 2015; pp 45–66.
- 380 (7) Dionne, J. A.; Sweatlock, L. A.; Atwater, H. A.; Polman, A. *Phys.*  
381 *Rev. B: Condens. Matter Mater. Phys.* **2006**, *73* (3), 035407.
- 382 (8) Bozhevolnyi, S. I.; Volkov, V. S.; Devaux, E.; Laluet, J.-Y.;  
383 Ebbesen, T. W. *Nature* **2006**, *440* (7083), 508–511.
- 384 (9) Dregely, D.; Lindfors, K.; Lippitz, M.; Engheta, N.; Totzeck, M.;  
385 Giessen, H. *Nat. Commun.* **2014**, *5*, 4354.
- 386 (10) Cohen, M.; Abulafia, Y.; Shavit, R.; Zalevsky, Z. *ACS Nano*  
387 **2017**, *11*, 3274.
- 388 (11) Carmeli, I.; Cohen, M.; Heifler, O.; Lilach, Y.; Zalevsky, Z.;  
389 Mujica, V.; Richter, S. *Nat. Commun.* **2015**, *6*, 7334.
- 390 (12) Cohen, M.; Shavit, R.; Zalevsky, Z.; Abulafia, Y. In *CLEO: 2014*;  
391 OSA Technical Digest (online); Optical Society of America, 2014; p  
392 JTu4A.135.
- 393 (13) Lu, H.; Liu, X.; Wang, G.; Mao, D. *Nanotechnology* **2012**, *23*  
394 (44), 444003.
- 395 (14) Wang, S.; Zhan, Q. *Sci. Rep.* **2016**, *6*, 29626.
- 396 (15) Choo, H.; Kim, M.-K.; Staffaroni, M.; Seok, T. J.; Bokor, J.;  
397 Cabrini, S.; Schuck, P. J.; Wu, M. C.; Yablonovitch, E. *Nat. Photonics*  
398 **2012**, *6* (12), 838–844.
- 399 (16) Wen, J.; Romanov, S.; Peschel, U. *Opt. Express* **2009**, *17* (8),  
400 5925–5932.
- 401 (17) Andryeuskii, A.; Zenin, V. A.; Malureanu, R.; Volkov, V. S.;  
402 Bozhevolnyi, S. I.; Lavrinenko, A. V. *Nano Lett.* **2014**, *14* (7), 3925–  
403 3929.
- 404 (18) Alù, A.; Engheta, N. *Phys. Rev. Lett.* **2010**, *104* (21), 213902.
- 405 (19) Solís, D. M.; Taboada, J. M.; Obelleiro, F.; Landesa, L. *Opt.*  
406 *Express* **2013**, *21* (2), 2369–2377.
- 407 (20) Dionne, J. A.; Sweatlock, L. A.; Sheldon, M. T.; Alivisatos, A. P.;  
408 Atwater, H. A. *IEEE J. Sel. Top. Quantum Electron.* **2010**, *16* (1), 295–  
409 306.
- 410 (21) Abediasl, H.; Hashemi, H. *Opt. Express* **2015**, *23* (5), 6509–  
411 6519.
- 412 (22) Cohen, E.; Ruberto, M.; Cohen, M.; Degani, O.; Ravid, S.;  
413 Ritter, D. *IEEE Trans. Microwave Theory Tech.* **2013**, *61* (3), 1359–  
414 1375.
- 415 (23) Sun, J.; Timurdogan, E.; Yaacobi, A.; Hosseini, E. S.; Watts, M.  
416 R. *Nature* **2013**, *493* (7431), 195–199.
- 417 (24) Maguid, E.; Yulevich, I.; Veksler, D.; Kleiner, V.; Brongersma,  
418 M. L.; Hasman, E. *Science* **2016**, *352*, 1202.
- 419 (25) Choi, H. S.; Kang, S. Y.; Cho, S. J.; Oh, I.-Y.; Shin, M.; Park, H.;  
420 Jang, C.; Min, B.-C.; Kim, S.-I.; Park, S.-Y.; Park, C. S. *Sci. Rep.* **2015**, *4*,  
421 5486.
- 422 (26) Yang, Y.; Li, Q.; Qiu, M. *Sci. Rep.* **2016**, *6*, 19490.